

Quantitative analysis of laser-generated ultrasonic wave characteristics and their correlation with grain size in polycrystalline materials

Zhaowen Xu(徐兆文), Xue Bai(白雪), Jian Ma(马健), Zhuangzhuang Wan(万壮壮), and Chaoqun Wang(王超群)
Citation: Chin. Phys. B, 2024, 33 (**8**): 087801. DOI: 10.1088/1674-1056/ad50bd

What follows is a list of articles you may be interested in

Gamma induced changes in Makrofol/CdSe nanocomposite films

Ali A. Alhazime, M. ME. Barakat, Radiyah A. Bahareth, E. M. Mahrous,Saad Aldawood, S. Abd El Aal, and S. A. Nouh
Chin. Phys. B, 2022, 31 (**9**): 097802. DOI: 10.1088/1674-1056/ac4909

Improving efficiency of inverted perovskite solar cells via ethanolamine-doped PEDOT:PSS as hole transport layer

Zi-Jun Wang(王子君), Jia-Wen Li(李嘉文), Da-Yong Zhang(张大勇), Gen-Jie Yang(杨根杰), and Jun-Sheng Yu(于军胜)
Chin. Phys. B, 2022, 31 (**8**): 087802. DOI: 10.1088/1674-1056/ac5988

On the structural and optical properties investigation of annealed Zn nanorods in the oxygen flux

Fatemeh Abdi
Chin. Phys. B, 2021, 30 (**11**): 117802. DOI: 10.1088/1674-1056/abf4ba

Ceramic synthesis of $0.08BiGaO_3$-$0.90BaTiO_3$-$0.02LiNbO_3$ under high pressure and high temperature

Hui Jin(金慧), Yong Li(李勇), Mou-Sheng Song(宋谋胜), Lin Chen(陈琳), Xiao-Peng Jia(贾晓鹏), Hong-An Ma(马红安)
Chin. Phys. B, 2016, 25 (**7**): 078202. DOI: 10.1088/1674-1056/25/7/078202

Soft magnetic properties of amorphous $Fe_{52}Co_{34}Hf_7B_6Cu_1$ alloy treated by pulsed magnetic field and annealing

Gu Yue (谷月), Chao Yue-Sheng (晁月盛), Zhang Yan-Hui (张艳辉)
Chin. Phys. B, 2012, 21 (**12**): 127805. DOI: 10.1088/1674-1056/21/12/127805

Quantitative analysis of laser-generated ultrasonic wave characteristics and their correlation with grain size in polycrystalline materials

Zhaowen Xu(徐兆文), Xue Bai(白雪)†, Jian Ma(马健), Zhuangzhuang Wan(万壮壮), and Chaoqun Wang(王超群)

Laser Institute, Qilu University of Technology (Shandong Academy of Sciences), Jinan 250104, *China*

(Received 28 December 2023; revised manuscript received 25 April 2024; accepted manuscript online 28 May 2024)

Quantitative relationship between nanosecond pulsed laser parameters and the characteristics of laser-generated ultrasonic waves in polycrystalline materials was evaluated. The high energy of the pulsed laser with a large irradiation spot simultaneously generated ultrasonic longitudinal and shear waves at the epicenter under the slight ablation regime. An optimized denoising technique based on wavelet thresholding and variational mode decomposition was applied to reduce noise in shear waves with a low signal-to-noise ratio. An approach for characterizing grain size was proposed using spectral central frequency ratio (SCFR) based on time-frequency analysis. The results demonstrate that the generation regime of ultrasonic waves is not solely determined by the laser power density; even at high power densities, a high energy with a large spot can generate an ultrasonic waveform dominated by the thermoelastic effect. This is ascribed to the intensification of the thermoelastic effect with the proportional increase in laser irradiation spot area for a given laser power density. Furthermore, both longitudinal and shear wave SCFRs are linearly related to grain size in polycrystalline materials; however, the shear wave SCFR is more sensitive to finer-grained materials. This study holds great significance for evaluating metal material properties using laser ultrasound.

Keywords: laser-ultrasonics, polycrystalline materials, ultrasonic time-frequency characteristics, grain size

PACS: 78.20.hc, 81.70.Cv, 43.35.Cg **DOI:** 10.1088/1674-1056/ad50bd

1. Introduction

Laser ultrasonic technique, as a rapidly evolving nondestructive testing (NDT) method, primarily utilizes a pulsed laser to generate ultrasonic waves and employs either a continuous or sufficiently long pulsed laser for detection.[1] Laser-generated ultrasound involves converting a portion of laser energy into thermal energy, resulting in localized temperature rise near the irradiated area and subsequent rapid thermal expansion. The commonly used laser source for ultrasonic wave generation is the *Q*-switched nanosecond pulsed Nd:YAG solid-state laser. Compared to traditional piezoelectric ultrasound techniques, laser ultrasound offers advantages such as long-distance and broadband detection capabilities even at high temperatures.[2–4] It is suitable for offline independent nondestructive testing of materials and especially online quality monitoring during metallurgical processes.[5–7]

Two distinct regimes for laser-generated ultrasonic waves are typically considered: a thermoelastic regime at low power densities and an ablation regime at high power densities. Theoretical models for laser-generated ultrasonic waves under the thermoelastic regime have been extensively studied. Researchers early assumed a tangential force source on the surface and obtained an analytical solution for the displacement field.[8] However, this assumption neglected the influence of thermal expansion effects and failed to account for how the size of the laser spot affects ultrasonic wave signals. Doyle *et al.*[9] pointed out that thermal expansion acted as a body force source, resulting in the precursor, i.e., longitudinal waves, due to the combined effect of tangential and body forces. McDonald *et al.*[10] discovered that the precursor was attributed to specific spatial scales of laser sources, indicating that an ideal point source would not generate the precursor. Nevertheless, quantitative analysis of the precursor could not be achieved using the body force source model alone. Furthermore, Sanderson *et al.*[11,12] proposed a model comprising a thermal dipole and a surface center of expansion, validated through finite element (FE) simulations and experimental findings. This model is the prevailing source model utilized in the context of the thermoelastic effect.

The application of higher incident laser power density leads to the generation of ultrasonic waves in the ablation regime, resulting from phenomena such as melting, vaporization, and plasma. The force source is commonly approximated as a time-varying force normal to the surface.[13] Hutchins *et al.*[14] have highlighted that the thermoelastic effect often accompanies the ablative regime. Therefore, the laser source comprises both a tangential force caused by the thermoelastic regime and a normal force caused by the ablative regime. Despite causing surface damage to the material, the ablation mechanism can generate ultrasonic signals with a high signal-to-noise ratio (SNR). This feature holds significant importance

†Corresponding author. E-mail: baixue0130@163.com

© 2024 Chinese Physical Society and IOP Publishing Ltd

for the online detection of metal processing in complex environments. For instance, the high SNR of laser ultrasonic signals under the ablation mechanism enables high-resolution detection of metallurgical defects during additive manufacturing, since the subsequent printing layer conceals any slight damage in the current one.[15]

The intermediate regime, also known as the slight ablation regime,[16] is characterized by a weak melting of the solid surface accompanied by a relatively noticeable thermoelastic effect. The force source in this regime consists of a normal force, thermal dipoles, and a surface center of expansion. Under this regime, the ultrasonic waveform exhibits similarities to that observed under the thermoelastic regime; however, there is a significant increase in the longitudinal wave amplitude.

The regimes mentioned above provide valuable insights into the intricate physical phenomena of laser-induced ultrasonic waves from the perspective of effective force sources. However, previous theoretical studies have not fully accounted for the effects of internal heat conduction and laser optical parameters on ultrasonic wave characteristics. Recently, Krylov *et al*.[17] proposed a more comprehensive theoretical model that integrates acoustics, optics, and material heat conduction. This model revealed that the previously used thermal dipole model has significant limitations in characterizing laser ultrasonic longitudinal waves. According to Krylov's model, the amplitude of these longitudinal waves was highly sensitive to the material's thermal properties and the reflectivity of its free surface under normal laser irradiation. However, to simplify calculations, the model omitted the small thermal expansion term associated with the material's elastic constants, limiting its ability to predict mechanical displacements accurately.

With the significant progress in computer technology, researchers have increasingly turned to FE simulation to better understand the characteristics of laser-induced ultrasonic waves.[18,19] In the thermoelastic mechanism, absorbed laser energy is typically converted into a heat source. Alternatively, in the ablation mechanism, a normal reaction force source exhibiting a spatial and temporal Gaussian distribution is often applied to the surface of the sample.[20] This simplification enables a thorough exploration of ultrasonic wave field directivity and propagation characteristics under different mechanisms. Furthermore, researchers are actively engaged in exploring how various pulsed laser parameters, including laser spot size,[21] penetration depth,[21] and laser beam profiles,[22] impact the ultrasonic wave field within materials. Their findings indicated that the directivity of laser-generated waves was influenced by the profile and size of the laser beam within the thermoelastic regime. Larger laser spots tended to narrow the main lobe of the wave field while having minimal effects on the side lobe. Moreover, researchers[23,24] have dedicated their efforts to elucidating the ultrasonic wave propagation characteristics. Their studies revealed that skimming longitudinal (SP) and skimming shear (SS) waves were particularly robust in the near field, distorting the surface wave's waveform.

The aforementioned research holds paramount importance for gaining a profound understanding of the generation and propagation of laser ultrasound. However, the intricate coupling between thermal and force sources remains underexplored. This coupling effect, particularly under the slight ablation mechanism, becomes increasingly complex and the analysis of ultrasonic shear wave characteristics in such scenarios remains inadequate. More importantly, previous experimental studies[25,26] have demonstrated that it is possible to modify the laser power density by adjusting the laser energy or irradiation spot diameter. It allows for generating an ultrasonic waveform dominated by thermoelastic effects at low power densities or an ablation-dominated ultrasonic waveform at high power densities. The ultrasonic generation mechanism has been demonstrated to be determined by the power density of the incident pulsed laser, as evidenced by numerous studies.[27,28] However, our preliminary experimental investigations have revealed that varying combinations of laser energy and irradiation spot diameter can generate ultrasonic waves under distinct regimes even when maintaining a constant power density. This observation may be attributed to the previously mentioned coupling effect between the thermal and force sources. Consequently, a thorough investigation of the mechanisms underlying laser-induced ultrasonic waves is imperative to achieve a more precise comprehension.

Furthermore, there has been insufficient research on laser-generated shear waves due to the lower SNR than longitudinal waves. Nevertheless, theoretical studies have confirmed that shear waves exhibit greater sensitivity towards microstructures in polycrystalline materials, particularly at lower frequencies. Therefore, the objective of this article is to comprehensively investigate the influence of various pulsed laser parameters, such as laser energy, irradiation spot diameter, and laser power density, on both the generation regime and time-frequency characteristics of laser ultrasonic waveforms. Special attention is devoted to analyzing shear wave characteristics. Additionally, we aim to elucidate the correlation between ultrasonic time-frequency characteristics and the grain size in polycrystalline materials.

This paper is organized as follows: The experimental methods are described in Section 2, and the denoising approach in Section 3. The time-frequency characteristics of ultrasonic signals under different incident pulse laser parameters are shown, and the quantitative relationship between them is established in Section 4. Subsequently, a grain size characterization method based on the downshift of ultrasonic spectral central frequency in the time-frequency domain is proposed,

and the corresponding experimental results are discussed in Section 5. The main conclusions are given finally.

2. Materials and experiments

The commercially pure titanium plate (99.5 wt% Ti) with dimensions of 200 mm × 100 mm was selected. Two specimens, varying in thickness, were prepared through a double annealing process involving an initial high-temperature annealing to achieve a fine-grained microstructure at the recrystallization temperature, followed by a subsequent low-temperature annealing.[29] Among these specimens, a 5-mm-thick one was designated for exploring ultrasonic longitudinal and shear wave characteristics. On the other hand, a 10-mm-thick specimen was chosen for studying surface wave properties, as this thickness helps to avoid interference from complex Lamb wave modes that can potentially occur in thinner plates.[23] Furthermore, four specimens with a thickness of 10 mm underwent heat treatment at 800 °C below the β-trans phase transition temperature for different durations of 0.5 h, 1.0 h, 2.0 h, and 8.0 h,[30] followed by air cooling to room temperature. Microstructural observations were conducted using electron backscatter diffraction (EBSD). The results revealed that the grains exhibited a nearly equiaxed morphology, and the average size was expressed as the mean grain diameter, yielding approximate values of 26 μm, 33 μm, 39 μm, and 49 μm. These results will be used for the correlation analysis between mean grain size and laser-ultrasonic characteristics.

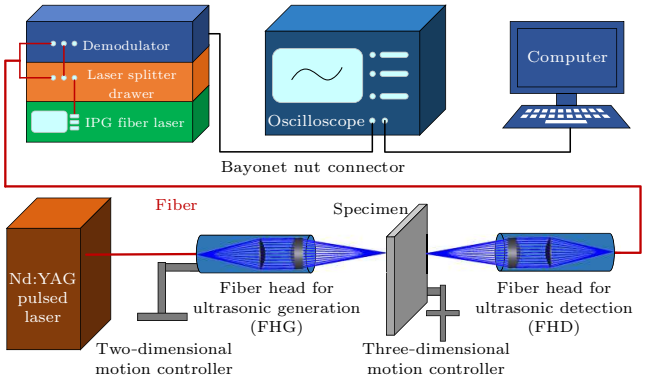


Fig. 1. Schematic diagram of laser ultrasonic inspection system.

The schematic diagram of the laser ultrasonic inspection system is depicted in Fig. 1. A pulsed laser beam, emitted by a Quantel Ultra 50 Nd:YAG solid-state laser with wavelength of 1064 nm and pulse width of 8 ns, is transmitted through an energy transfer fiber. Subsequently, it is transformed into a focused laser spot via collimating and focusing lenses before being incident onto the specimen's surface. The collimating and focusing lenses are combined to form a fiber head for ultrasonic generation (FHG), fixed on the two-dimensional motion controller. The power density of the pulsed laser exhibits a spatial Gaussian distribution with its amplitude at the center of the irradiation spot expressed by $I_0 = E/(\tau A)$.[31] E and τ denote the incident laser energy and pulse width, respectively. A is the irradiation spot area. It should be noted that the absorbed power density I_a by the material is determined by multiplying the incident power density I_0 with the material's optical absorption coefficient γ[32] and can be expressed as $I_a = I_0\gamma$. An AIR-1550-TWM receiver based on two-wave mixing (TWM) interference provided by Intelligent Optical Systems, Inc., equipped with a detection bandwidth ranging from 20 kHz to 125 MHz, is utilized for laser-ultrasonic wave detection.

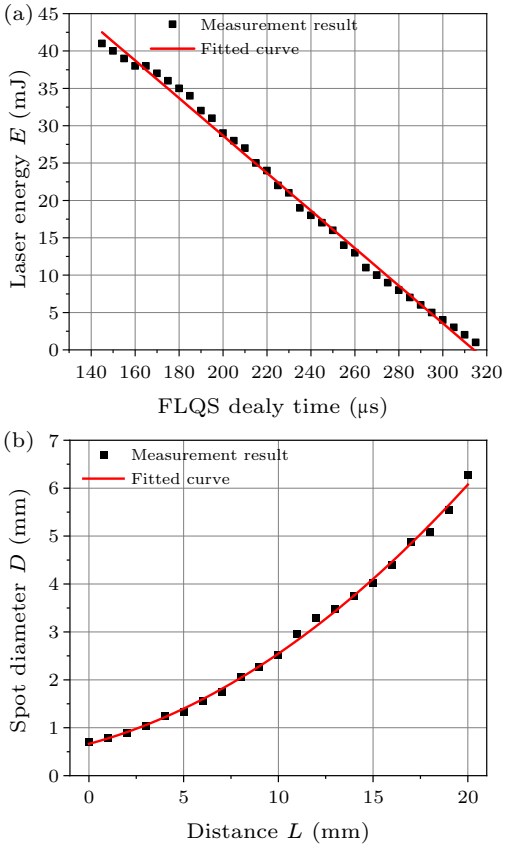


Fig. 2. Interrelation of spatiotemporal modulation parameters of the pulsed laser: (a) corresponding to the relation between the incident laser energy (E) and FLQS delay time with its linear fitting, (b) corresponding to the relation between irradiated spot diameter (D) and the distance (L) between the specimen and the focus point of FHG, which is captured through a polynomial fitting.

The ultrasonic surface wave is detected on the same side as the laser incident surface. A detection distance of at least 5 mm from the incident point is advisable for accurate surface wave detection to eliminate any interference from SP and SS waves.[23] In contrast, the ultrasonic longitudinal and shear waves are received at the epicenter on the opposite side with collinearity between the incident and detection points. It is imperative to attain the shortest arrival time of the initial longitudinal pulse to ensure the precision of the collinearity. The ultrasonic signal in the time domain is stored after averaging 128 times to reduce high-frequency electrical noises.

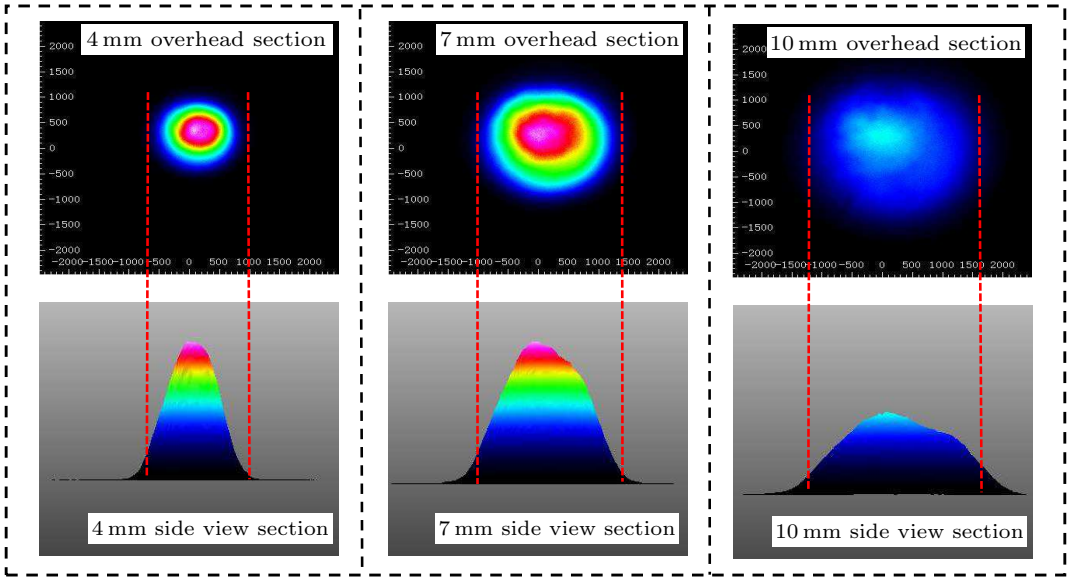


Fig. 3. The overhead (upper) and side (lower) view sections of the laser irradiation spot at different distances of L, obtained by the BC106N-VIS/M beam quality analyzer from Thorlabs.

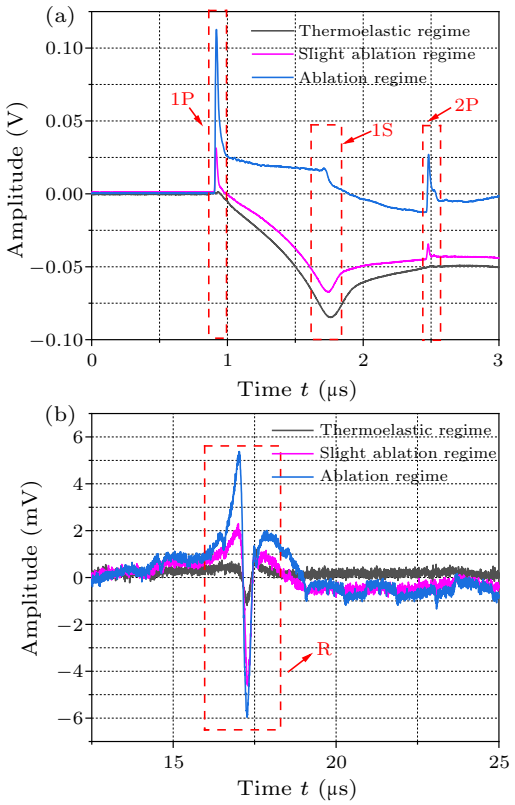


Fig. 4. Typical laser ultrasonic waveforms under the thermoelastic, slight ablation, and ablation regimes: (a) ultrasonic longitudinal and shear bulk waves detected at the epicenter, and (b) ultrasonic surface waves detected 51 mm away from the incident point.

The experiments are designed based on the principle of manipulating a single variable to investigate the impact of various laser parameters, such as laser energy, irradiated spot diameter, and laser power density, on the characteristics of ultrasonic waves. The laser energy is controlled by manipulating the flashlamp-to-Q-switch (FLQS) delay time. The Labmax top laser power meter from coherence measures the laser energy at different FLQS delay times. The relationship between laser energy and FLQS delay times is illustrated in Fig. 2(a), demonstrating a strong negative linear correlation with a high goodness of fit ($R^2 > 0.99$). The linear slope is -0.25 mJ/μs, indicating that the laser energy decreases by 0.25 mJ for every 1 μs increment in FLQS delay time. Notably, as the delay time increases from 140 μs to 315 μs, there is a corresponding decrease in laser energy from 41 mJ to 1 mJ. On another note, the irradiated spot diameter D is controlled by the distance of the specimen to the focus of FHG, denoted as L. The spot diameters at different distances are measured using an BC106N-VIS/M beam quality analyzer from Thorlabs. The relationship between D and L is depicted in Fig. 2(b), which can be accurately described by a quadratic polynomial $D = 8.23(L + 6.44)^2 + 321.88$. This suggests that the irradiated spot diameter exhibits an approximate square correlation with the distance from the FHG focus to the workpiece. In particular, an increase in L from 0 to 20 mm leads to a corresponding increase in D from 0.71 mm to 6.27 mm.

The cross-sectional images of the laser irradiation spots at various distances, obtained using the beam quality analyzer, are presented in Fig. 3. The top-view cross section reveals that the irradiated spot exhibits an approximately circular shape for distances less than 4 mm. Radially, the intensity distribution follows a Gaussian-like pattern with maximum intensity at its center. As we move the specimen away from FHG's focus, aberrations occur in both the spot shape and the Gaussian intensity distribution, decreasing intensity at the spot center. These aberrations become more pronounced as the distance L increases.

3. Optimized SWT-VMD signal denoising

The typical laser ultrasonic waveforms in titanium alloy plates under the thermoelastic, intermediate, and ablation

regimes are depicted in Fig. 4 as the black, magenta, and blue curves, respectively. Ultrasonic longitudinal (P), shear (S), and surface waves (R) are denoted. The initial and secondary longitudinal pulse echoes transmitted from the bottom surface are represented by 1P and 2P. In Fig. 4(a), under the thermoelastic regime, 1P and 2P pulses exhibit relatively low amplitudes with a prominent negative step-like feature after the arrival of 1P, followed by an evident positive shear pulse. The ultrasonic waveform under the slight ablation regime resembles the thermoelastic regime but with an increased amplitude for 1P and 2P. However, the ultrasonic waveforms exhibit notable distinctions in the ablation regime as compared to previous regimes. The emergence of a significant positive pulse, known as the 1P pulse, elicits a positive step-like response instead of a negative one. The 2P pulse shows a good SNR, while shear wave pulses only appear as simple slope changes.[33] Compared to ultrasonic longitudinal and shear waves, ultrasonic surface waves show significant polarity variations depending on the generation regime.[34] It can be observed in Fig. 4(b) that, under the thermoelastic and slight ablation regimes, they exhibit unipolar behavior, while under the ablative regime, they become bipolar.

3.1. SWT-based initial signal denoising

Since a broadband TWM interferometer is utilized, the acquired signals typically contain grain scattering-induced noises and high-frequency electrical noises resulting from the generation process of laser ultrasound. Therefore, it is crucial to denoise the signal effectively. The stationary wavelet transform (SWT) possesses time-frequency local adaptability, making it particularly suitable for non-stationary and nonlinear laser ultrasonic signals. Three steps for SWT denoising are described as follows: (1) Selecting the Daubechies' least-asymmetric wavelet, referred to as Sym$N$, as the basis function for decomposing the ultrasonic signal. Here, N represents the number of vanishing moments. It is imperative to consider several crucial factors, including its regularity, support width, and similarity to the signal for the selection of the vanishing moment. After weighing all these factors, it is selected to be 7 to guarantee optimal performance in signal denoising and reconstruction. This choice of wavelet helps mitigate phase distortion caused by signal denoising and reconstruction processes. The decomposition level, denoted by m, is critical to distinguishing noise components from actual signals. The decomposition yields approximation coefficients (low-frequency components) and detail coefficients (high-frequency components). (2) Employing soft thresholding technique to eliminate detail coefficients smaller than a given threshold value. (3) Obtaining a noise-reduced signal through wavelet reconstruction using approximation coefficients from level m and detail coefficients from levels ranging from 1 to m processed by the soft thresholding method. Figures 5(a) and 5(b) illustrate the decomposition results of an ultrasonic waveform at the epicenter, dominated by thermoelastic effects, with a level m equal to 4 and 5, respectively. It is evident that when $m = 5$, significant longitudinal wave components are captured in detail coefficients at the fifth level while the approximate component loses part of effective signals accordingly. Henceforth, an optimal decomposition level is set to 4.

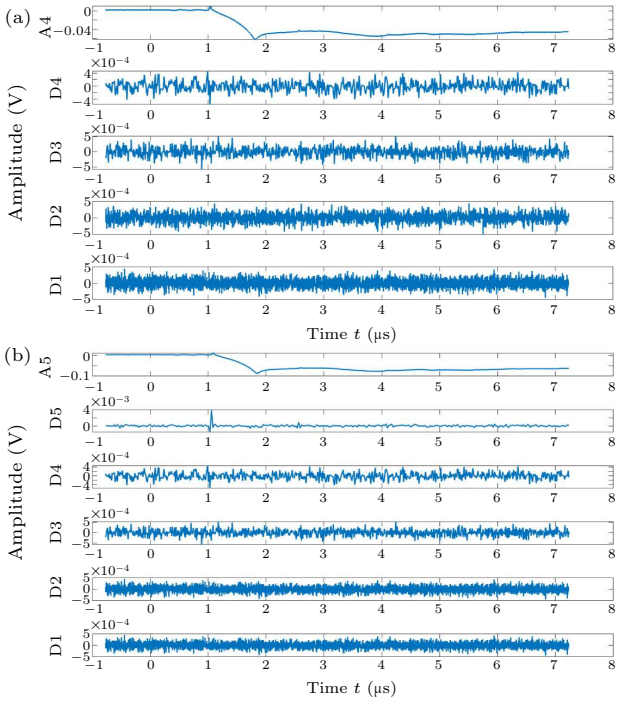


Fig. 5. The decomposition results of laser ultrasonic waveform at the epicenter using the SWT with different decomposition levels m: (a) $m = 4$. (b) $m = 5$.

The continuous wavelet transform (CWT) based on a complex Morlet (Cmor) wavelet is applied to the denoised signal to capture the frequency components at each moment. The optimal bandwidth and central frequency of the Cmor wavelet are determined by Shannon wavelet entropy[35] as 2.6 and 0.4, respectively. Figures 6(a)–6(c) exhibit the wavelet time-frequency images for ultrasonic longitudinal, shear, and surface waves, respectively, acquired with the laser energy of 24 mJ and the spot diameter of 0.71 mm. Their spectrum curves at the arrival time of the pulse peak are plotted in Figs. 7(a)–7(c). The spectra of longitudinal and surface waves show approximately the Gaussian distribution, indicating that SWT denoising effectively suppresses their high-frequency noise components. However, the spectrum of shear waves has deviated considerably from the Gaussian distribution, and there are high-frequency noises exceeding 10 MHz. This indicates that the SWT method has failed to effectively reduce noise in shear wave signals. Actually, the SNR of the ultrasonic shear wave (2.3 dB) is significantly lower than those of the initial longitudinal waves (34.8 dB) and surface waves (25.5 dB). This highlights the necessity for further denoising techniques to enhance shear wave signals with a low SNR.

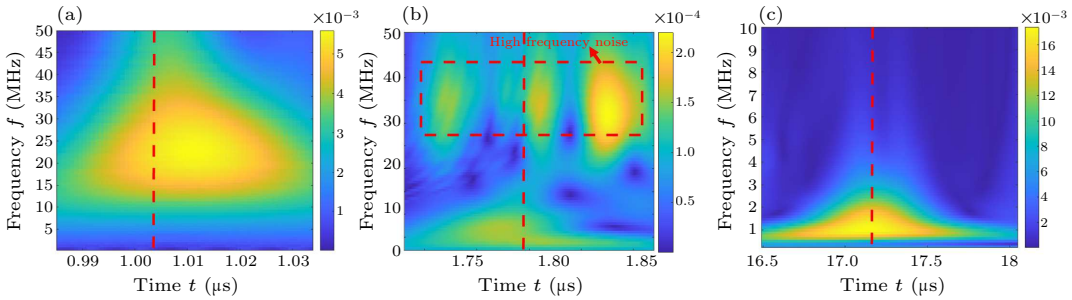


Fig. 6. Wavelet time-frequency images for three different wave modes: (a) longitudinal waves, (b) shear waves, (c) surface waves.

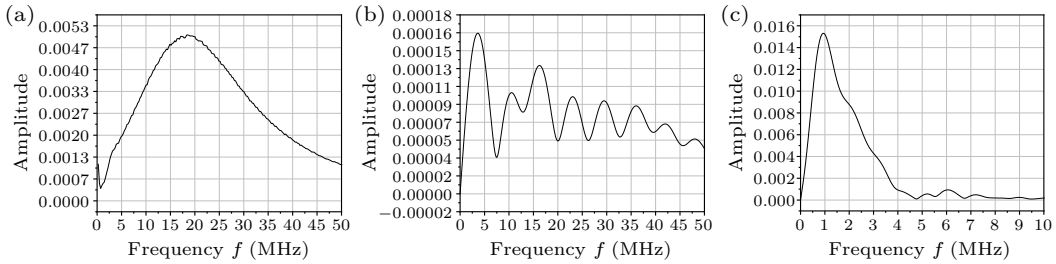


Fig. 7. Spectrum curves derived from Fig. 6 at the pulse peak arrival time for three ultrasonic wave modes: (a) longitudinal waves, (b) shear waves, (c) surface waves.

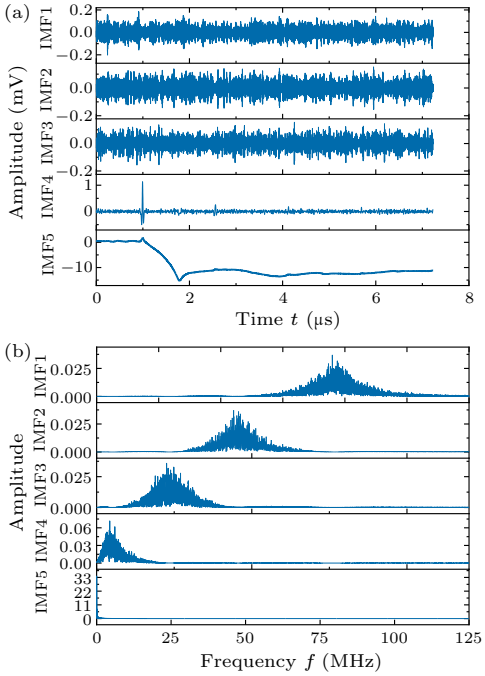


Fig. 8. The VMD-based IMFs in the time domain and their spectral amplitudes: (a) IMFs in the time domain, (b) spectral amplitudes of IMFs.

3.2. VMD-based further signal denoising

Variational mode decomposition (VMD) is an adaptive and fully non-recursive technique suitable for signal denoising.[36] Based on the VMD, the signal is decomposed into multi-order intrinsic mode functions (IMFs). The k-th order IMF is denoted as IMFk, where $k = 1, 2, \ldots, K$. The IMFs with the highest order K of 5 are depicted in Figs. 8(a) and 8(b), showcasing their results in both the time and frequency domains, respectively. It can be observed that VMD aims to decompose signals into components with varying center frequencies, wherein the central frequency decreases as the order of IMF increases. The lower-order IMFs represent high-frequency noise components, while the higher-order IMFs mainly capture practical signal components. The key to VMD-based denoising is identifying and eliminating high-frequency noise components across all IMFs. Previous research has demonstrated that there exists a constant relationship between the product of energy density (E_{dk}) dominated by noises in an IMF and its mean period (T_k),[37] which can be defined by

$$E_{\mathrm{dk}} = \frac{1}{J}\sum_{j=1}^{J}(\mathrm{IMF}k_j)^2, \tag{1}$$

$$T_k = \frac{2J}{\mathrm{Optima}_k}, \tag{2}$$

where J is the length of an IMF, and Optima_k denotes the total number of extreme points within IMFk.

Figure 9(a) illustrates the variation of the product $E_{\mathrm{dk}}T_k$ concerning the order k. Considering that the energy from noise components is significantly smaller than the signal's energy, we can identify the order in which the product exhibits rapid growth as a demarcation between noise and signal components. Expressly, IMF1–IMF3 represent noise components, while IMF4 and IMF5 correspond to practical signal components. Consequently, a further denoised signal can be obtained through reconstruction based on IMF4 and IMF5. The time-frequency image of the shear wave obtained through the SWT-VMD combination denoising approach is presented in Fig. 9(b). Comparing the result in Fig. 6(b), it becomes evident that high-frequency noises have been substantially eliminated, thereby highlighting the detailed features of shear waves.

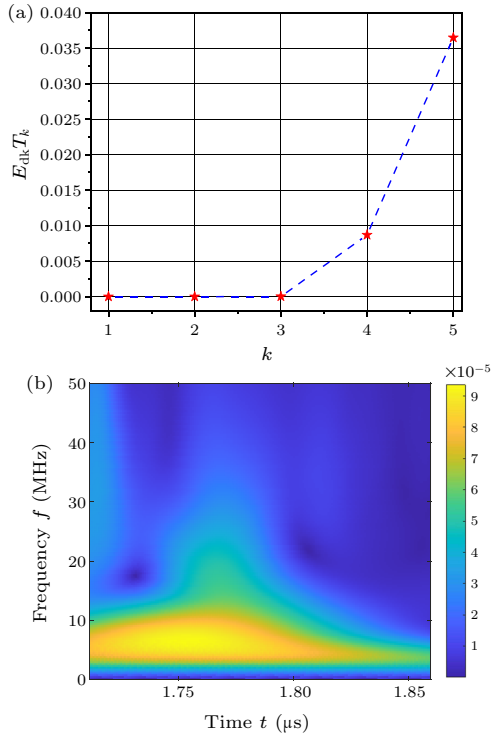


Fig. 9. Results of shear wave denoising by the SWT-VMD combination approach: (a) corresponding to the product of energy density and its mean period in an IMF, $E_{dk}T_k$, concerning the order k, and (b) corresponding to the CWT time-frequency image of the denoised shear wave.

4. Results and discussions on laser-generated ultrasonic wave characteristics

4.1. Effects of pulsed laser energy on ultrasonic characteristics

To explore the impact of the pulsed laser energy on ultrasonic characteristics, the distance between the FHG and the test specimen is set equal to the focal length, ensuring a consistent irradiation spot diameter of $D = 0.71$ mm. This guarantees that the sole variable is the pulsed laser energy, which gradually increased in 1 mJ increments within the range of 1–41 mJ. The surface diagrams of the ultrasonic waveforms are presented in Fig. 10, illustrating the variation of laser energy from 1 mJ to 41 mJ. Specifically, Figs. 10(a) and 10(b) depict ultrasonic bulk waves, encompassing both longitudinal and shear waves, and surface waves, respectively. Enlarged views of ultrasonic longitudinal and shear waves can be observed in Figs. 10(c) and 10(d), respectively. These three wave modes exhibit notably different trends in both amplitude and polarity. The longitudinal pulse remains positive, exhibiting an amplitude increase of around 62 times from 1.1 mV to 68.5 mV. The shear pulse transits from a positive step-like waveform due to thermoelastic effects to a pattern characterized by a slope change in the ablation regime. Its maximum amplitude reaches as high as 29.2 mV, approximately 17 times higher than its minimum counterpart. Meanwhile, the ultrasonic surface wave transforms from unipolarity in the thermoelastic regime to bipolarity under the ablation regime, with an amplitude increase of around six times from 1.7 mV to 11.2 mV.

It is worth noting that a transient local temperature rise occurs in the material at low incident laser energy, resulting in no damage to the material's surface [Fig. 11(a)]. A gradual increasing of the incident laser power leads to surface melting of the material, causing white marks to appear in the laser irradiation area [Fig. 11(b)]. Further increase in incident laser power causes some materials to vaporize and ionize, generating plasma and exhibiting strong ablative effects [Fig. 11(c)].

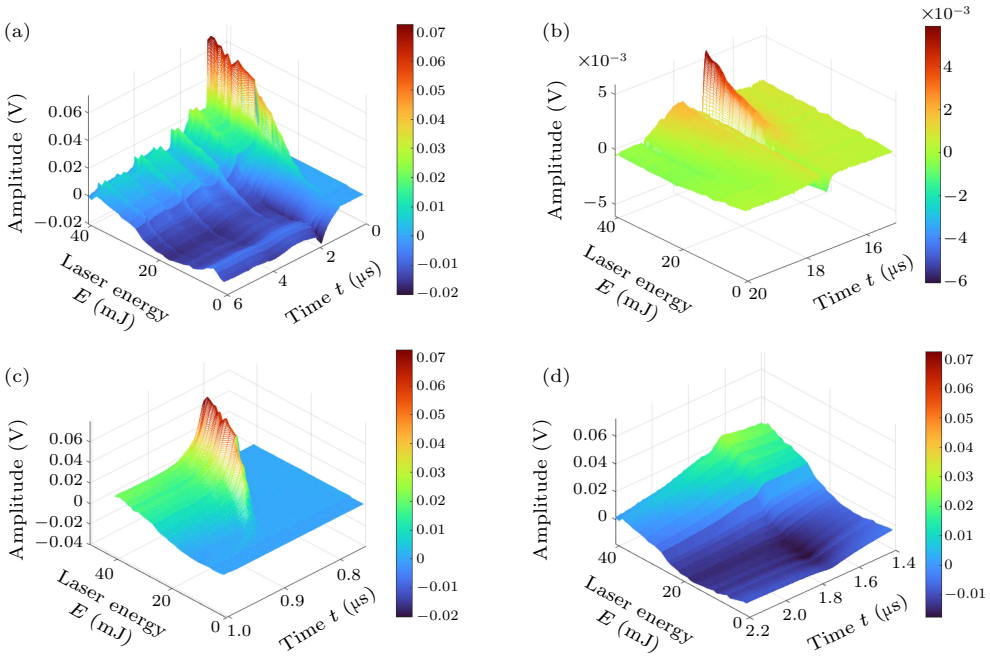


Fig. 10. Surface diagrams of the ultrasonic waveforms versus incident laser energy from 1 mJ to 41 mJ: (a) ultrasonic bulk waves, (b) ultrasonic surface wave, (c) enlarged view of initial longitudinal pulses, (d) enlarged view of shear pulses.

The laser shot causes approximately a maximum of 0.15 mm of surface damage under this regime, advancing by no more than 0.05 μs in the arrival time of longitudinal pulses [as shown in Fig. 10(c)].

The spectral surface diagram of three wave modes, obtained by Fourier transform as a function of laser energy, is illustrated in Fig. 12. As the laser energy increases, the maximum amplitude of longitudinal and surface waves continuously rises, while the amplitude of shear waves initially increases, then decreases, and eventually increases again. At a given laser energy level, all three wave modes exhibit Gaussian distribution shapes with goodness-of-fit values exceeding 0.85. However, the center frequencies of longitudinal, shear, and surface waves differ significantly at 22 MHz, 3 MHz, and 1 MHz, respectively. The −6 dB bandwidth for longitudinal waves is 29 MHz, considerably higher than that for shear and surface waves.

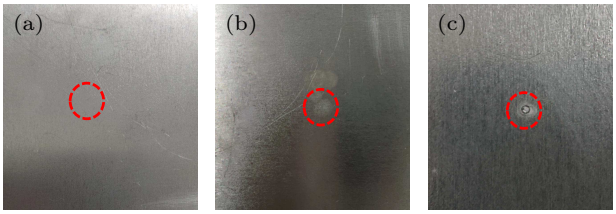


Fig. 11. Sample surface after the pulsed laser incident under different mechanisms: (a) thermoelastic mechanism, (b) slight ablation mechanism, (c) ablation mechanism.

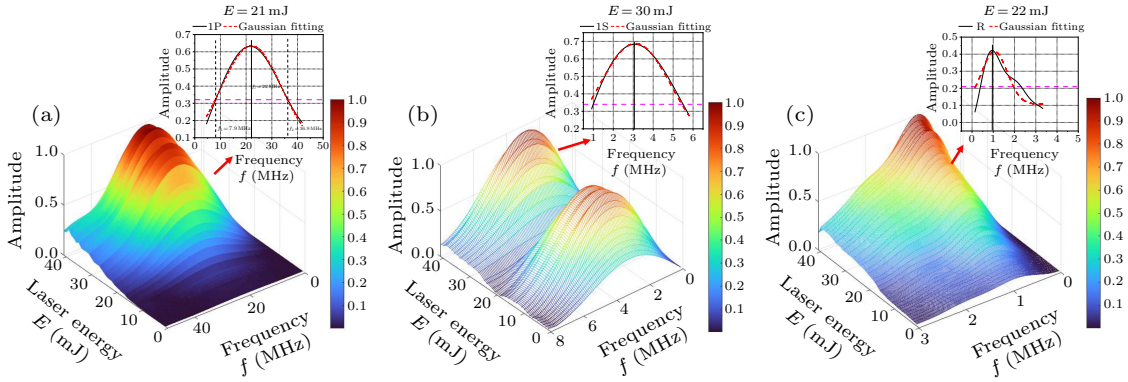


Fig. 12. The spectral surface diagram based on the Fourier transform as a function of laser energy for different modes of ultrasonic waves: (a) longitudinal waves, (b) shear waves, (c) surface waves.

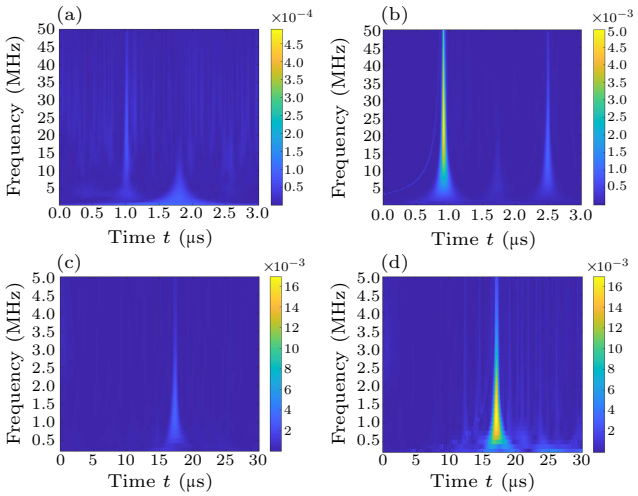


Fig. 13. CWT-based time-frequency diagrams of laser ultrasonic bulk waves under (a) thermoelastic and (b) ablation regimes, as well as surface waves detected 51 mm away from the incident point under (c) thermoelastic and (d) ablation regimes. The waveforms under the thermoelastic and ablation regimes were obtained by the incident laser energies of 6 mJ and 23 mJ.

Time-frequency analysis can effectively describe the subtle characteristic changes due to the broadband, transient, and nonlinear nature of laser ultrasonic signals. Taking the examples of laser energies of 6 and 23 mJ (corresponding to thermoelastic and ablation regimes, respectively), figure 13 presents time-frequency diagrams of laser ultrasonic waveforms. The horizontal axis represents time, the vertical axis represents frequency, and the color indicates wavelet coefficients. The central frequency of the spectrum corresponds to the frequency at which the maximum wavelet coefficient occurs. Regarding the ultrasonic bulk wave in the thermoelastic regime, figure 13(a) demonstrates that the maximum wavelet coefficient occurs at the arrival time of the shear pulse peak and its spectral central frequency of 3 MHz. Conversely, the ablation regime shown in Fig. 13(b) reveals that the maximum wavelet coefficient occurs at the arrival time of the longitudinal pulse peak and its spectral central frequency of 21 MHz. It suggests that shear waves have higher energy than longitudinal waves in the thermoelastic regime, and vice versa for the ablation regime. For ultrasonic surface waves under thermoelastic and ablative regimes, maximum wavelet coefficients appear at their respective surface wave peaks with a spectral central frequency of 1 MHz. Nevertheless, the maximum value achieved under the ablation regime is seven times greater than that obtained from the thermoelastic regime.

Compared to the amplitude analysis, ultrasonic wave energy analysis demonstrates robustness against random noises and transient fluctuations. Figure 14 presents the variations of ultrasonic wave energy concerning laser energy in time, frequency, and time-frequency domains for three wave modes. Additionally, it showcases the piecewise linear fitting of the average results across these three domains by

the magenta solid lines. The energy of a wave mode in the time domain is calculated by summing up the squared amplitudes at each sampling time within $[t_0, t_1]$, defined by $E_U = \{\sum_{n=1}^{n=N}[x(t_n)]^2\Delta t\}/R'$, where $x(t)$ and Δt denote the time-domain signal and the sampling time interval. Here t_0 and t_1 denote the arrival and ending times of the pulse echo, and R' represents the impedance. The wave energy in the frequency domain is expressed as $E_U = \{\sum_{n'=1}^{n'=N'}[x(f_{n'})]^2\Delta f\}/R'$, where the spectrum of $x(f)$ is based on Fourier transform, Δf denotes the frequency interval; f_1 and f_2 denote starting and end cutoff frequencies corresponding to the -6 dB bandwidth. The wave energy in the time-frequency domain is determined by summing up squared wavelet coefficients within $[t_0, t_1]$ and $[f_1, f_2]$, given by $E_U = \{\sum_{n'=1}^{n'=N'}[\sum_{n=1}^{n=N}[W(t_n, f_{n'})]^2\Delta t]\Delta f\}/R'$. Each curve in Fig. 14 is normalized by its maximum energy value. For a given wave mode, consistent variation trends between laser energy and ultrasonic wave energy are observed across different domains.

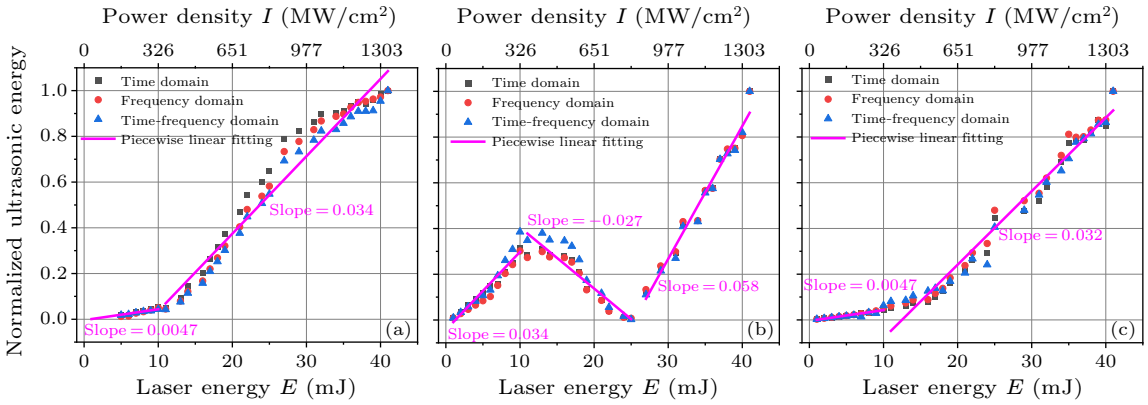


Fig. 14. The variations of ultrasonic wave energy concerning laser energy with the piecewise linear fitting for three different wave modes: (a) longitudinal waves, (b) shear waves, (c) surface waves.

As the incident laser energy increases, longitudinal and surface waves exhibit a piecewise linear growth trend in ultrasonic wave energy. The ultrasonic wave energy gradually increases with a linear growth slope of approximately 0.0047 mJ^{-1} for laser energies below 12 mJ. In comparison, it undergoes a rapid escalation with a slope of around 0.034 mJ^{-1} when the incident laser energy exceeds 12 mJ. The physical interpretation of a slope equal to k_{slope} is that the generated p-wave energy increases by $100k_{\text{slope}}$ percent relative to its maximum value for every 1 mJ increase in the incident laser energy. Obviously, for both the longitudinal and surface waves, the growth slope of ultrasonic energy under the ablation mechanism is significantly higher than that under the thermoelastic mechanism. Nevertheless, the underlying reasons for these two wave modes are not identical.

In the case of longitudinal waves [Fig. 14(a)], this phenomenon can be attributed to variations in the directivity of the ultrasonic p-wave across different regimes. Specifically, at lower incident laser energies, the generation of ultrasonic signals primarily stems from thermoelastic effects. The maximum amplitude of the p-wave is observed at an angle approximately equal to 50° and propagates outward in a single lobe form. Its amplitude at the epicenter is minimal. There is a gradual shift in directivity towards the normal direction during the transition from thermoelastic to ablative regimes. Under ablative conditions, the maximum amplitude of the p-wave occurs at the epicenter, resulting in a rapid increase. Regarding the surface wave [Fig. 14(c)], the energy distribution exhibits no significant directivity in the case of a pulsed laser source with a point-like configuration. It is approximately uniform along the circumference regardless of whether it is generated under thermoelastic or ablative regimes. Unlike p-waves, the change in polarity leads to an increase in the energy growth slope.

Compared to longitudinal and surface waves, the energy of shear waves exhibits a complex variation trend [Fig. 14(b)]. It can be divided into three stages: (1) For laser energy below 12 mJ, a more prominent amplitude component can be detected at the epicenter due to the thermoelastic effect. The wave energy increases gradually with a slope of 0.034 mJ^{-1} as the laser energy increases. (2) When the laser energy ranges from 12 mJ to 25 mJ, along with shear wave generation predominantly driven by the slight ablation regime, the wave energy at the epicenter gradually weakens, and its directivity shifts towards angles 30°–60°. Therefore, it is observed that s-wave energy decreases linearly with a slope of -0.027 mJ^{-1}. (3) The ablation effect gradually intensifies for laser energies exceeding 25 mJ, resulting in an incremental increase in the energy of shear waves with a slope of 0.058 mJ^{-1}.

4.2. Effects of irradiation spot diameter on ultrasonic characteristics

In order to investigate the impact of laser irradiation spot diameter on ultrasonic characteristics, a fixed incident laser energy of 36 mJ is taken as an example. The ultrasonic waveforms are obtained by varying the distance L between the specimen and the focus point of FHG in equal intervals of 1 mm

within the range of [0, 20 mm] [Figs. 15(a)–15(c)]. Consequently, the corresponding laser power density decreases from 1144 MW/cm^2 to 15 MW/cm^2. The normalized ultrasonic energy for each wave mode, relative to its maximum amplitude, is plotted against the diameter of the laser irradiation spot [Figs. 16(a)–16(c)].

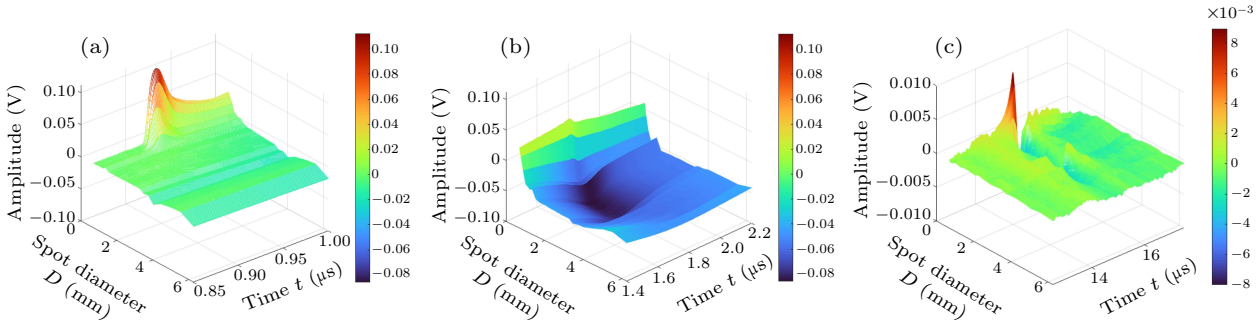


Fig. 15. Time-domain ultrasonic signals concerning the laser irradiation spot diameter for different wave modes: (a) longitudinal waves, (b) shear waves, (c) surface waves.

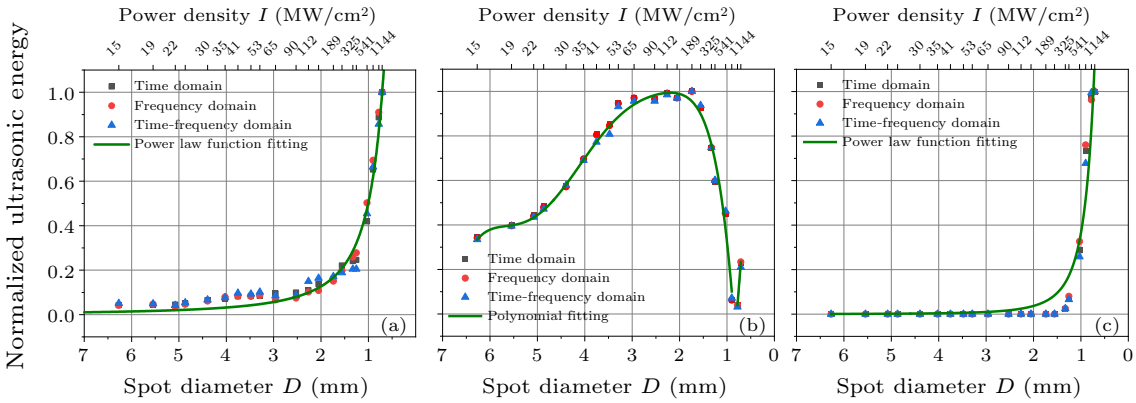


Fig. 16. The normalized ultrasonic energy relative to its maximum amplitude in different domains (time, frequency, and time-frequency) concerning the laser irradiation spot diameter for three wave modes, and their non-linear fitting results: (a) longitudinal waves, (b) shear waves, (c) surface waves.

When L exceeds 6 mm, the irradiation spot's diameter exceeds 1.74 mm, while maintaining a laser power density below 236 MW/cm^2. As the diameter of the irradiation spot decreases, there is a slight increase in ultrasonic energies for longitudinal and surface waves. In contrast, the energy of ultrasonic shear waves initially increases and then stabilizes. Within the range of [1.0, 1.74] mm for D (corresponding to an increase in L from 2 to 6 mm), the slight ablation becomes the dominant regime for ultrasonic generation, resulting in a gradual rise in energies for both longitudinal and surface waves but a rapid decline in transverse wave energy. At $L = 0$, i.e., when the focus of FHG is located on the incident surface of the specimen, an instantaneous increase in laser power density up to 1144 MW/cm^2 leads to significant ablation on the surface material. The energy of the three wave modes increases, with the longitudinal and surface waves exhibiting more pronounced increments. Notably, within laser spot diameters ranging from 0.71 mm to 6.27 mm, variations in longitudinal wave energy are more pronounced with a maximum-to-minimum ratio reaching up to 80. However, this ratio reaches only up to approximately 15.5 and 23.8 for shear and surface waves, respectively. It should be emphasized that maximum energies are achieved by longitudinal and surface waves when $L = 0$, whereas the shear wave attains its maximum value at $L = 6$ mm. A sixth-degree polynomial fitting provides relatively accurate curves describing variations in shear wave's energy levels, while power-function fitting yields relatively accurate curves for longitudinal and surface waves with the power exponent of approximately -3.3 and -2.0, respectively.

4.3. Effects of laser power density on ultrasonic characteristics

Based on the above-mentioned points, it appears that ultrasonic characteristics are determined by pulsed laser power density when either laser energy or irradiation spot diameter changes independently. However, various combinations of laser energy and irradiated spot diameter may exist for a given laser power density, such as high-energy/large-spot and low-energy/small-spot. Ten different laser power densities are used for conducting laser ultrasonic experiments to investigate their effects on ultrasonic characteristics. Each power density considers two configurations associated with higher-energy/larger-spot and lower-energy/smaller-spot. The parameters for the pulsed laser are presented in Table 1.

Table 1. Parameters of the incident pulsed laser. E_a and D_a denote the combination of high-energy/large-spot, E_b and D_b denote the combination of low-energy/small-spot.

I_0 (MW/cm^2)	20	40	60	80	100	120	140	160	180	200
E_a (mJ)	26	41	21	36	41	24.4	28.4	40	36	41
D_a (mm)	4.6	4.0	2.4	2.7	2.6	1.8	1.8	2.0	1.8	1.8
E_b (mJ)	2.8	6	6	11	14	16	21	26	26	24
D_b (mm)	1.5	1.5	1.2	1.5	1.5	1.5	1.5	1.5	1.5	1.4

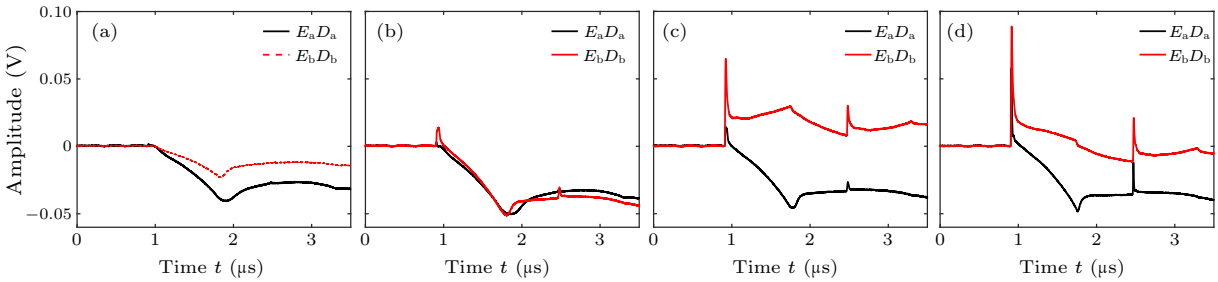


Fig. 17. The laser ultrasonic bulk waves obtained at four different laser power densities: (a) 20 MW/cm^2, (b) 120 MW/cm^2, (c) 160 MW/cm^2, (d) 200 MW/cm^2.

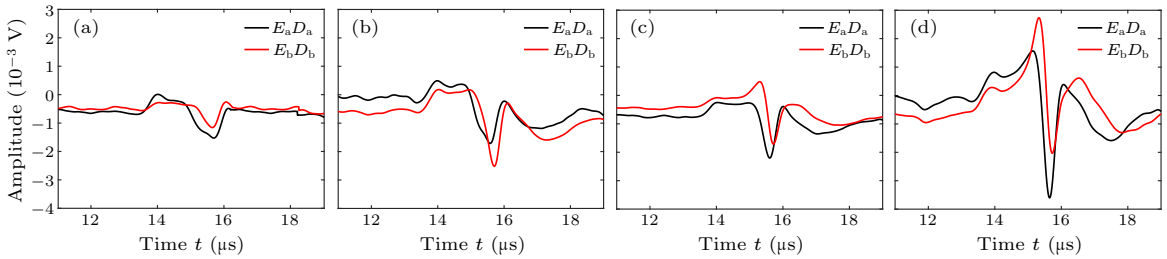


Fig. 18. The laser ultrasonic surface waves detected 47 mm away from the incident point at four different laser power densities: (a) 20 MW/cm^2, (b) 120 MW/cm^2, (c) 160 MW/cm^2, (d) 200 MW/cm^2.

The laser ultrasonic bulk waveforms obtained at four different laser power densities (20 MW/cm^2, 120 MW/cm^2, 160 MW/cm^2, and 200 MW/cm^2) are illustrated in Fig. 17. As depicted in Fig. 17(a), when the incident laser power density is set to 20 MW/cm^2, both high-energy/large-spot and low-energy/small-spot configurations generate ultrasonic waveforms predominantly governed by the thermoelastic regime. However, the shear wave amplitude generated by high-energy/large-spot is greater. With increasing power density, the distinction between ultrasonic waveforms generated by these two configurations becomes more pronounced. At an incident laser power density of 120 MW/cm^2 [Fig. 17(b)], the ultrasonic waveform produced by the low-energy/small-spot configuration exhibits a significant increase in longitudinal amplitude, indicating a typical waveform characterized by the slight ablation regime. At an incident laser power density of 160 MW/cm^2 [Fig. 17(c)], the shear amplitude of ultrasonic waveforms generated by the low-energy/small-spot configuration decreases significantly with a slope tendency, suggesting typical ablation-dominated waveforms. At an incident laser power density of 200 MW/cm^2 [Fig. 17(d)], the shear wave stimulated by low-energy/small-spot shows a change in slope trend with an increasing amplitude, which indicates a strong ablation regime accompanied by plasma. In contrast, for laser power densities below or equal to 160 MW/cm^2, the high-energy/large-spot configuration consistently generates typical thermoelastic waveforms. Only when reaching an incident laser power density of 200 MW/cm^2 does it become evident that there is a noticeable increase in longitudinal wave amplitude stimulated by highenergy/largespot, indicating the generation regime changes to the slight ablation.

Figures 18(a)–18(d) demonstrate the evolution of ultrasonic surface waveforms across various laser power densities. The polarity of the surface wave is consistent with the generation regimes for both configurations mentioned in the above analysis. Notably, at the lowest power density of 20 MW/cm^2 [Fig. 18(a)], both configurations produce unipolar waveforms, indicating the dominance of the thermoelastic mechanism. Conversely, at the highest power density of 200 MW/cm^2 [Fig. 18(d)], both configurations exhibit bipolar waveforms, signifying the transition into the strong-ablation mechanism. However, when considering the power densities of 120 MW/cm^2 [Fig. 18(b)] and 160 MW/cm^2 [Fig. 18(c)], the two different configurations exhibit distinct regimes despite the same power density. Specifically, the low-energy/small-spot combination undergoes a transition from the slight ablation to the ablation mechanism, marked by a significant increase in amplitude and a shift towards a bipolar

waveform. In contrast, the high-energy/large-spot combination maintains the thermoelastic waveform, primarily exhibiting an increase in amplitude.

The ultrasonic energies in the time-frequency domain as a function of laser power density for three different wave modes are depicted in Figs. 19(a)–19(c). The solid line with squares represents the results for high energy/large spot, while the solid line with circles corresponds to those of low energy/small spot. The results for each wave mode have been normalized by their respective maximum values.

Regarding longitudinal waves [Fig. 19(a)], when the incident power density is below 120 MW/cm^2, they manifest as precursors with low amplitudes. As the laser power density increases, the ultrasonic energy remains stable, and there is no discernible distinction in the wave energy excited by high-energy/large-spot and low-energy/small-spot. In the range of laser power densities from 120 MW/cm^2 to 180 MW/cm^2, the ultrasonic energy generated by high-energy/large-spot excitation remains steady due to thermoelastic effects. It shows an increasing trend at an incident power density exceeding 180 MW/cm^2, indicating a shift in the generation regime. On the other hand, ultrasonic energy produced by low-energy/small-spot excitation starts to increase at a laser power intensity of 120 MW/cm^2, suggesting a transition from thermoelastic to ablative regimes. It exhibits continuous rapid growth in ultrasonic energy corresponding to an intense ablation regime accompanied by plasmas for incident power densities exceeding 180 MW/cm^2.

The ultrasonic surface wave [Fig. 19(c)] exhibits an increasing trend in ultrasonic energies with the rise of laser power density for both high-energy/large-spot and low-energy/small-spot generations. A careful comparison reveals that at incident power densities below 100 MW/cm^2, the high-energy/large-spot generation yields a more incredible ultrasonic energy. However, when the incident power densities exceed 100 MW/cm^2, high-energy/large-spot and low-energy/small-spot generations produce equally matched ultrasonic energies.

Regarding shear waves [Fig. 19(b)], as the laser power density increases, the overall ultrasonic energy stimulated by high-energy/large-spot generation surpasses that stimulated by low-energy/small-spot generation. It is primarily due to the dominance of the thermoelastic regime in generating relatively significant amplitude at the epicenter when the laser power density is less than 180 MW/cm^2. However, contrary to the variation trend in Fig. 16(b), the shear wave energy exhibits irregular fluctuations for both configurations. Simultaneous irregular variations in laser energy and irradiation spot diameter may explain the irregular fluctuations.

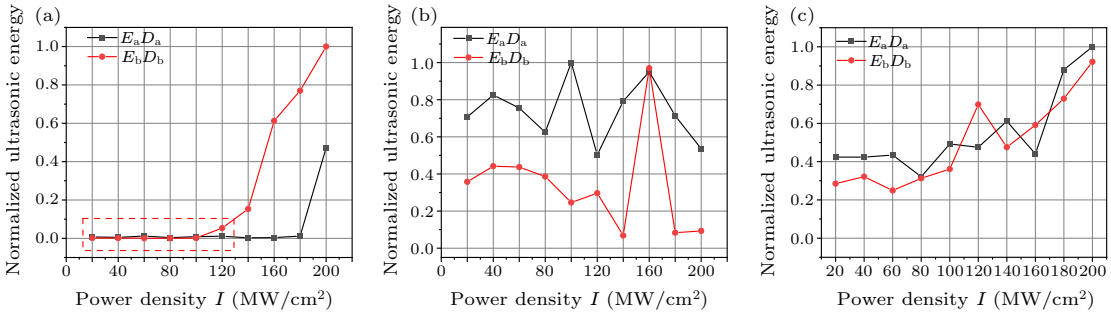


Fig. 19. Ultrasonic energies in the time-frequency domain as a function of laser power density for three different wave modes: (a) longitudinal waves, (b) shear waves, (c) surface waves.

Based on the above analysis, it is observed that high-energy/large-spot excitation leads to a characteristic waveform in the thermoelastic regime. In contrast, low-energy/small-spot excitation produces a typical waveform in the ablative regime within a laser power density range of 120–180 MW/cm^2. This phenomenon will be elucidated from the perspective of the thermoelastic generation regime. When a pulsed laser irradiates a localized surface area of a metal sample, part of the laser energy elevates the temperature at a specific depth beneath the irradiated surface. This transient increase in local temperature induces thermal expansion and generates an elastic wave under the thermoelastic effect. Within this thermoelastic regime, we can consider the source as a central expansion source consisting of three equal orthogonal force dipoles given by[11,12]

$$D_{11} = D_{22} = D_{33} = B\delta V, \tag{3}$$

where $B = \lambda + 2/3\mu$ is the bulk modulus of elasticity with λ and μ denoting the material's Lamé constants, and δV denotes the change in solid volume. The resulting strain field is defined as

$$\varepsilon_{11} = \varepsilon_{22} = \varepsilon_{33} = \frac{1}{3}\frac{\delta V}{V}, \tag{4}$$

$$\frac{\delta V}{V} = 3\beta\delta T, \tag{5}$$

$$\delta T = \frac{\gamma I_0}{\rho C \delta z}. \tag{6}$$

Here, β is the linear expansion coefficient, and δz denotes the depth of the region where temperature rises beneath the surface. Here ρ and C denote the material's density and specific heat capacity; δT signifies the temperature increase when subjected to an incident laser power density I_0 and irradiation area A. V denotes the total volume of the temperature rise area, given by $V = A\delta z$. Therefore, by substituting Eq. (6) into Eq. (5), we obtain

$$\delta V = \frac{3\beta\gamma I_0 A}{\rho C}. \tag{7}$$

According to Eq. (7), it is evident that the thermoelastic effect induces a volume change in the expansion source, which is directly proportional to the radiation area at a specific laser power density. It implies that the thermoelastic effect becomes more pronounced for a given laser power density as the laser irradiation spot area increases. This observation elucidates why high-energy/large-spot generation results in a waveform dominated by the thermoelastic effect. It should be noted that the strain caused by the thermoelastic effect, i.e., $\delta V/V$, remains constant for identical laser power densities. This research holds significance in generating ultrasonic longitudinal and shear waves simultaneously through higher laser energy with larger irradiation spots, thereby facilitating precise detection of metallurgical characteristics such as defects through superimposing ultrasonic longitudinal and shear waves.

5. Laser ultrasonic characterization for grain size in polycrystalline materials

5.1. Correlation between ultrasonic characteristics and grain size of materials

Further analysis is conducted on the correlation between the time-frequency characteristics of laser ultrasonic signals and the grain size of material microstructures. The aim is to provide an empirical foundation for characterizing material microstructure. Previous studies have demonstrated that when an incident ultrasonic signal has an amplitude spectrum conforming to a Gaussian distribution, its amplitude spectrum maintains a Gaussian shape after propagation for a certain distance. However, due to the more significant attenuation of high-frequency components compared to low-frequency components, the central frequency of the power spectrum shifts downwards.

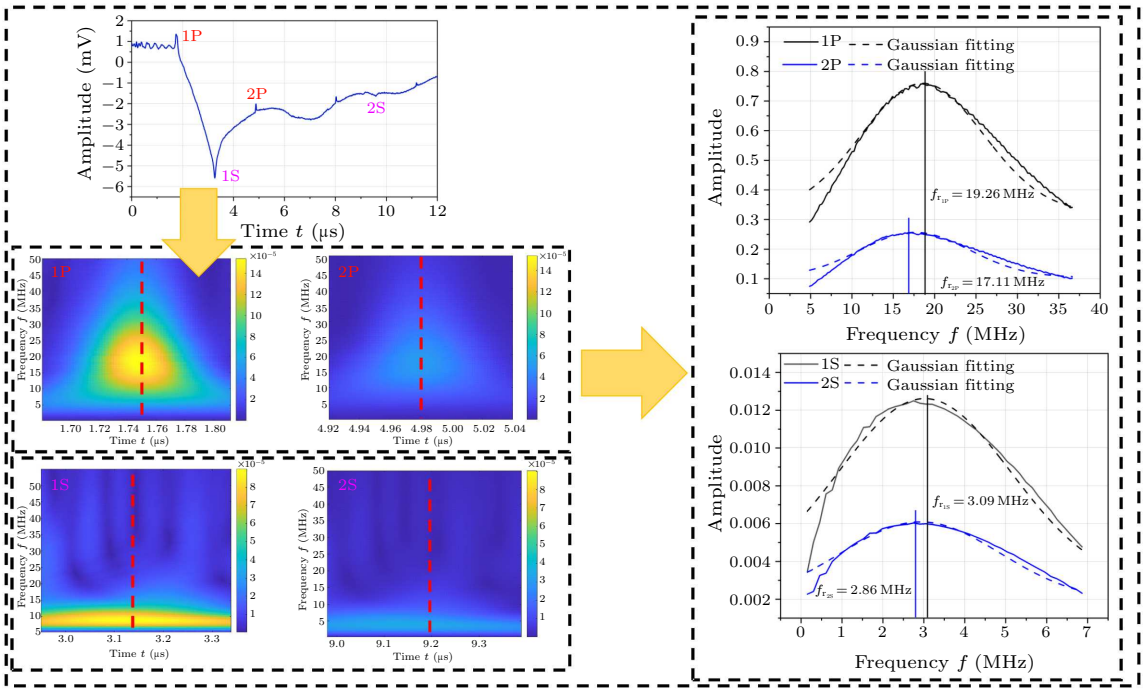


Fig. 20. Calculation of central frequency downshift based on time-frequency analysis.

Actually, the attenuation induced by grain scattering, quantified by a scalar coefficient, α, is assumed to be proportional to the $(n-1)$th power of the mean grain size d and to the n-th power of the frequency f. The power index n is dependent on the ratio of the mean grain size d to the wavelength λ. Notably, within the practical and frequently utilized ranges of ultrasonic wavelength and grain size, the Rayleigh-to-stochastic scattering transition region, characterized by $n \approx 2$, is a particularly common occurrence. Under this assumption, the attenuation can be expressed by $\alpha = \alpha_0 f^2$, where $\alpha_0 = bd$ denotes the frequency-independent attenuation coefficient. It has been shown that α_0 is proportional to the grain size, where b represents the linearly proportional coefficient relating to the elastic constants and density of materials. Consequently, the spectral

central frequency ratio (SCFR) between successive two pulse echoes exhibits a linear relationship with the mean size d of microstructure grains:[38]

$$f_{r1}/f_{r2} = 2\sigma_{r1}^2 z\alpha_0 + 1 = 2\sigma_{r1}^2 zbd + 1, \tag{8}$$

where f_{r1} and f_{r2} are the center frequencies of the first and second pulse echoes, z is the propagation distance, and σ_{r1}^2 is the spectrum variance of the first pulse echo. This method demonstrates less sensitivity towards wave diffraction, reflection, and transmission effects than traditional ultrasonic attenuation methods. The accuracy in measuring spectral central frequency shift is crucial. However, standard deviations in multiple measurements based on Fourier transform spectra can be significant, resulting in reduced accuracy in characterizing grain size.

Considering the superior ability of time-frequency images to capture instantaneous spectral changes of laser ultrasonic signals, this paper proposes an approach to characterize grain size by evaluating the downshift in central frequency by analyzing the signal spectrum at the arrival time of ultrasonic pulse peaks obtained via time-frequency analysis. To compare the effectiveness of longitudinal and shear waves in characterizing the mean grain size, simultaneous generation of these two wave modes is achieved with high laser energy and large spot size. A laser energy is set at 41 mJ, and a spot diameter is set at 2.96 mm, resulting in the corresponding laser power density of 74.5 MW/cm^2. The obtained laser ultrasonic waveform is shown in Fig. 20. After denoising through the SWT-VMD technique, the rectangular window function intercepts 1P, 2P, 1S, and 2S pulses for CWT analysis to obtain wavelet time-frequency images. Spectral curves corresponding to peak arrival times (1.75 μs for 1P signal, 4.98 μs for 2P signal, 3.13 μs for 1S signal, and 9.16 μs for 2S signal) are plotted in Fig. 20. Nonlinear regression fitting using the Gaussian model is employed to determine center frequencies.

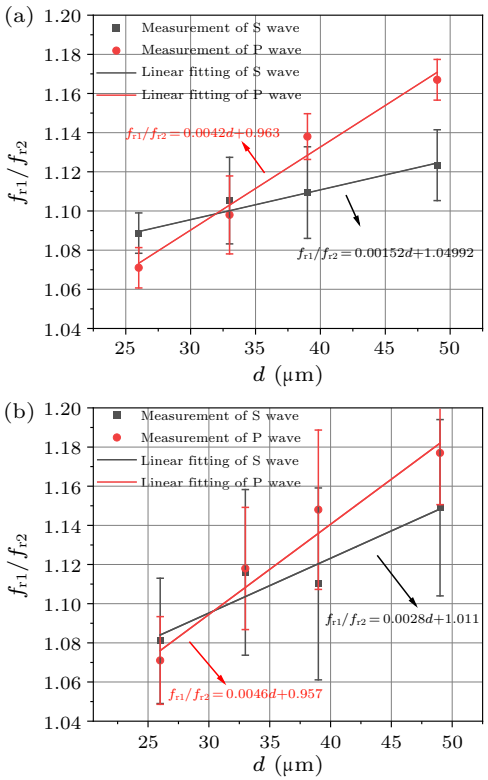


Fig. 21. The SCFR between the successive two pulse echoes, concerning the average grain sizes in titanium alloys for longitudinal and shear waves: (a) time-frequency analysis using CWT, (b) spectral analysis employing Fourier transform.

Table 2. Comparisons in the SCFR between the longitudinal and shear waves.

Mean grain sizes (μm)	Time-frequency analysis based on CWT				Spectral analysis based on FFT			
	SCFRs of P-wave		SCFRs of S-wave		SCFRs of P-wave		SCFRs of S-wave	
	Mean value	Standard deviation	Mean value	Standard deviation	Mean value	Standard deviation	Mean value	Standard deviation
26	1.071	0.0123	1.089	0.0103	1.071	0.0224	1.081	0.0320
33	1.098	0.0219	1.105	0.0221	1.118	0.0312	1.116	0.0423
39	1.138	0.0117	1.109	0.0234	1.148	0.0407	1.110	0.0490
49	1.167	0.0114	1.123	0.0181	1.177	0.0264	1.149	0.0450

Ten points with a spacing interval of more than 2 mm were selected on the surface of samples with mean grain sizes of 26 μm, 33 μm, 39 μm, and 49 μm for laser ultrasonic detection. The wavelet time-frequency analysis method was used to evaluate the averaged result and standard deviation of SCFR for both longitudinal and shear waves, as plotted against mean grain size in Fig. 21(a). The circle and square symbols represent the measured mean values of SCFR for longitudinal and shear waves, respectively. Error bars indicate standard deviations from multiple measurements. Red and black solid lines show linear fitting results for longitudinal and shear waves, respectively. Results reveal that both longitudinal and shear wave SCFRs increase linearly with grain size, with the p-wave proportionality coefficient nearly three times of that for shear waves based on the time-frequency analysis. However, careful comparison shows that samples with larger grain sizes ($>$ 32 μm) have more significant SCFRs in longitudinal waves. In comparison, those with finer grains ($<$ 32 μm) have more significant SCFRs in shear waves. This suggests that characterization precision based on shear wave spectra is higher for smaller grain sizes and vice versa for larger ones. The comparison with traditional Fourier spectrum analysis (as shown in Fig. 21(b) and Table 2) reveals that the standard deviation obtained through Fourier spectrum analysis is approx-

imately three times higher than the results obtained through CWT analysis. Additionally, due to the low SNR, the standard deviation of SCFRs is higher in ultrasonic shear wave pulse echoes than those from longitudinal pulse echoes.

5.2. Grain size evaluation based on SCFR obtained by time-frequency analysis

According to Eq. (8), the grain size can be characterized by analyzing its linear correlation with the SCFR in the time-frequency domain. Note that the accurate estimation of the linear coefficient b is crucial for characterizing grain size. Conventionally, this coefficient can be estimated using classical theoretical attenuation models.[39] However, these models often overlook the crucial influence of grain size distribution, which can have a significant impact on the spatial correlation function, accordingly altering the ultrasonic attenuation level. To improve the accuracy of estimating the linear coefficient, this paper adopts the analytical model proposed by Turner *et al.*[40] This model incorporates the log-normal distribution of grain sizes into the calculation of attenuation, providing a more realistic representation of grain size distribution in polycrystalline materials.

According to Turner's model, the attenuation can be described as the summation of two components. One component represents the attenuation caused by scattering into the same wave mode as the incident one (indicated by α_{LL} for longitudinal waves, and α_{TT} for shear waves), while the other signifies the scattering resulting from mode conversion (indicated by α_{LT} for longitudinal waves and α_{TL} for shear waves):

$$\alpha_{\mathrm{L}} = \alpha_{\mathrm{LL}} + \alpha_{\mathrm{LT}}, \tag{9a}$$

$$\alpha_{\mathrm{T}} = \alpha_{\mathrm{TT}} + \alpha_{\mathrm{TL}}, \tag{9b}$$

with

$$\alpha_{\mathrm{LL}} = \frac{k_{\mathrm{L}}^4 \pi}{4 v_{\mathrm{L}}^4 \rho^2} \int_0^{\pi} \eta(\theta_{\mathrm{ps}}) M_1(\theta_{\mathrm{ps}}) \sin\theta_{\mathrm{ps}} \,\mathrm{d}\theta_{\mathrm{ps}}, \tag{10a}$$

$$\alpha_{\mathrm{LT}} = \frac{k_{\mathrm{T}}^4 \pi}{4 v_{\mathrm{L}}^3 v_{\mathrm{T}} \rho^2} \int_0^{\pi} \eta(\theta_{\mathrm{ps}}) [M_2(\theta_{\mathrm{ps}}) - M_1(\theta_{\mathrm{ps}})] \sin\theta_{\mathrm{ps}} \,\mathrm{d}\theta_{\mathrm{ps}}, \tag{10b}$$

$$\alpha_{\mathrm{TL}} = \frac{k_{\mathrm{L}}^4 \pi}{8 v_{\mathrm{T}}^3 v_{\mathrm{L}} \rho^2} \int_0^{\pi} \eta(\theta_{\mathrm{ps}}) [M_2(\theta_{\mathrm{ps}}) - M_1(\theta_{\mathrm{ps}})] \sin\theta_{\mathrm{ps}} \,\mathrm{d}\theta_{\mathrm{ps}}, \tag{10c}$$

$$\alpha_{\mathrm{TT}} = \frac{k_{\mathrm{T}}^4 \pi}{8 v_{\mathrm{L}}^4 \rho^2} \int_0^{\pi} \eta(\theta_{\mathrm{ps}}) [M_3(\theta_{\mathrm{ps}}) - 2M_2(\theta_{\mathrm{ps}}) + M_1(\theta_{\mathrm{ps}})] \sin\theta_{\mathrm{ps}} \,\mathrm{d}\theta_{\mathrm{ps}}. \tag{10d}$$

The subscripts L and T denote longitudinal and shear waves, respectively; M_1, M_2, and M_3 denote the covariance inner product of elastic constants of the material, which are related to the incident and scattering wave modes as defined in Refs. [40,41]. Here, v_ξ and k_ξ represent the phase velocity and wave number, respectively, of the ultrasonic wave mode ξ; θ_{ps} refers to the angle between the incident and scattered waves. The spatial correlation function, denoted by $\eta(\theta_{\mathrm{ps}})$, quantifies the probability of any two points in space belonging to the same grain. It can be expressed as an integral of the average chord length l, formulated as

$$\eta(\theta_{\mathrm{ps}}) = \int_0^{\infty} P(l) \frac{l^3}{\pi^2 [1 + l^2 (k_{\mathrm{i}}^2 + k_{\mathrm{s}}^2 + 2 k_{\mathrm{i}} k_{\mathrm{s}} \cos\theta_{\mathrm{ps}})]^2} \,\mathrm{d}l. \tag{11}$$

It is noteworthy that the correlation between l and grain size remains undefined and is currently an active area of investigation; l can be approximated as the radius of equiaxed grains with an assumption of Poisson statistics; k_{i} and k_{s} denote the wave numbers of the incident and scattered wave modes, respectively. $P(l)$ denotes the volume fraction of each grain size and is expressed for a lognormal distribution as follows:

$$P(l) = \frac{1}{l \sigma_{\mathrm{d}} \sqrt{2\pi}} \exp\left(- \frac{(\ln l - \mu_{\mathrm{d}})^2}{2 \sigma_{\mathrm{d}}^2} \right), \tag{12}$$

where μ_{d} and σ_{d} denote the mean value and standard deviation. Given the knowledge of these two parameters, the attenuation coefficient at a specific frequency can be numerically estimated based on Eqs. (9)–(12).

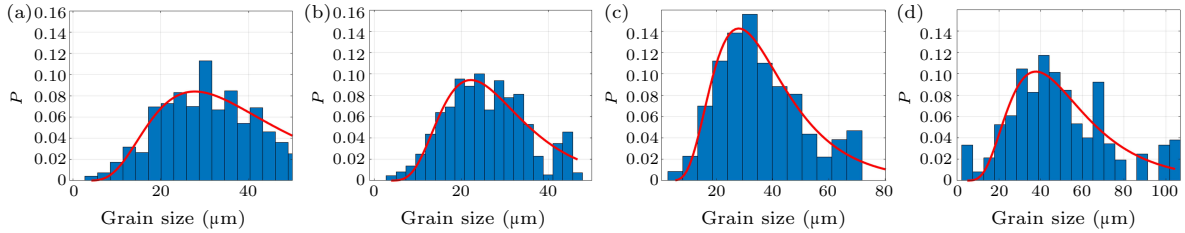


Fig. 22. The blue histograms depicting the grain size distribution for all samples featuring various mean grain diameters (d), and their log-normal distribution fitting represented by the red curve: (a) $d = 26$ μm, (b) $d = 33$ μm, (c) $d = 39$ μm, (d) $d = 49$ μm.

Based on EBSD microstructural observations, the grain size distribution histograms for all samples are plotted as blue bar charts in Fig. 22. Subsequently, a log-normal distribution fitting is conducted, and the fitted curve is represented by a red solid line. The analysis indicates that the root-mean-square errors (RMSE) of the log-normal distribution fitting for the grain size distribution across all samples are no more than 0.02. The pertinent fitting parameters μ_{d} and σ_{d} are listed in

Table 3. They were incorporated into Eqs. (9)–(12) to compute the attenuation in various samples at a given frequency f_0. Then, the proportionality coefficients b can be approximated at the frequency f_0 by employing the linear fitting between the predicted attenuation coefficients and the mean grain size obtained through EBSD. Note that the linear relation assumption holds approximately within a specific frequency range. To achieve a closer alignment with this linear relationship, we choose three frequencies that are proximate to the central frequency for a specific wave mode and calculate their respective linear coefficients b. Finally, the average value of b across these frequencies is used for grain size evaluation.

Table 3. The microstructure data observed through EBSD analysis, along with the fitted parameters derived from a log-normal distribution of grain sizes.

Annealed temperature/Holding time	Data obtained by EBSD analysis	Best-fit log-normal distributions		
	d (μm)	σ_d	μ_d	RMSE (10^{-2})
800 °C/0.5 h	26	0.42	−10.24	1.44
800 °C/1.0 h	33	0.50	−10.54	1.34
800 °C/2.0 h	39	0.46	−10.27	1.51
800 °C/8.0 h	49	0.48	−9.95	2.04

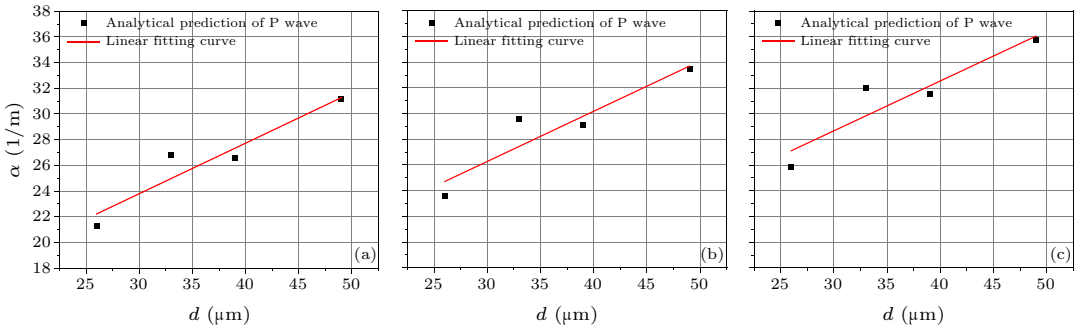


Fig. 23. Linear fitting between the predicted attenuation by Turner's model and the mean grain size obtained by EBSD for longitudinal waves at three different frequencies: (a) 18 MHz, (b) 19 MHz, (c) 20 MHz.

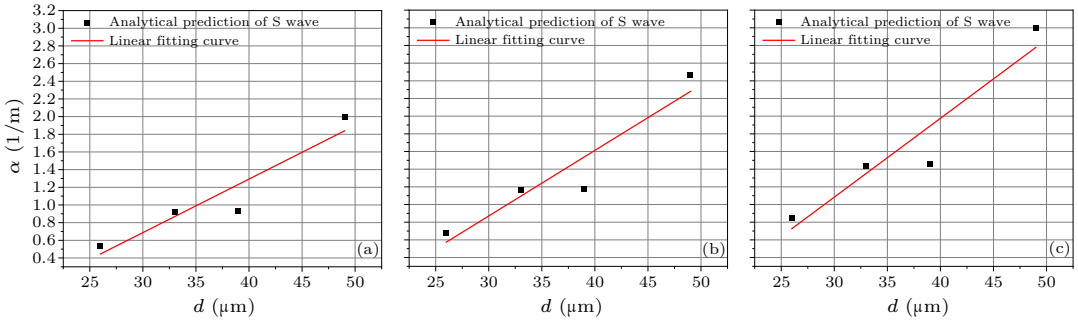


Fig. 24. Linear fitting between the predicted attenuation by Turner's model and the mean grain size obtained by EBSD for shear waves at three different frequencies: (a) 2.8 MHz, (b) 3.0 MHz, (c) 3.2 MHz.

Specifically, for longitudinal waves, three frequencies of 18 MHz, 19 MHz, and 20 MHz were chosen, while for shear waves, frequencies of 2.8 MHz, 3.0 MHz, and 3.2 MHz were selected. The attenuation coefficients at these frequencies were calculated for all samples. They are then plotted against the mean grain diameter measured by EBSD, as indicated by solid squares for longitudinal and shear waves in Figs. 23 and 24, respectively. The linear fitting results reveal that the goodness of fit (R^2) exceeds 0.9 for both wave modes. Based on the slopes of the fitted linear curves, the proportionality coefficients for longitudinal waves are determined to be 1.62×10^{-9} s^2/m^2, 1.07×10^{-9} s^2/m^2, and 1.25×10^{-9} s^2/m^2 at the respective frequencies, averaging to 1.31×10^{-9} s^2/m^2. For shear waves, the proportionality coefficients were 7.73×10^{-9} s^2/m^2, 8.24×10^{-9} s^2/m^2, and 8.71×10^{-9} s^2/m^2 at the respective frequencies, averaging to 8.23×10^{-9} s^2/m^2. Finally, the average grain size of each sample is nondestructively evaluated using Eq. (8), factoring in the estimated linear coefficient b, as well as the SCFR outlined in Table 2. The evaluation outcomes obtained using laser-ultrasonic longitudinal and shear waves are presented in Table 4.

The experimental results reveal that when predicting the grain size of coarse-grained samples ($d > 32$ μm), the accuracy of longitudinal waves significantly surpasses that of shear waves. Notably, the maximum error for longitudinal waves is merely 4.03%, whereas the maximum error for shear waves reaches 9.85%. Both errors were observed in samples

with a mean grain size of 39 μm. However, the situation reverses when predicting the grain size of fine-grained samples ($d < 32$ μm), with shear waves exhibiting superior prediction accuracy compared to longitudinal waves. In this case, the prediction errors by longitudinal and shear waves in samples with a grain size of 26 μm are 4.84% and 6.38%, respectively. These experimental findings align well with the observations detailed in Subsection 5.1, indicating that a larger downshift in the central frequency of consecutive pulse echoes in the time-frequency domain corresponds to greater scatter-induced attenuation, resulting in smaller prediction errors for the corresponding grain size. Conversely, a smaller downshift in the central frequency is associated with larger prediction errors.

Table 4. Comparison of the mean grain sizes measured by laser-ultrasonics with those observed through EBSD.

Annealed temperature/ Holding time	EBSD observation results (μm)	Results estimated by longitudinal waves		Results estimated by shear waves	
		Results (μm)	Error (%)	Results (μm)	Error (%)
800 °C/0.5 h	26	24.34	6.38	24.74	4.84
800 °C/1.0 h	33	32.28	2.18	31.24	5.3
800 °C/2.0 h	39	40.57	4.03	35.16	9.85
800 °C/8.0 h	49	45.03	2.11	43.63	4.84

6. Conclusions

In summary, we have investigated the impact of nanosecond pulsed laser parameters on the generation regime and time-frequency characteristics of ultrasonic waves in metals and alloys. The main conclusions are as follows:

(1) When maintaining a constant irradiation spot diameter, the energies of ultrasonic longitudinal and surface waves demonstrate a piecewise linear growth as the incident pulsed laser energy increases. Notably, the linear growth rates observed under the slight ablation and ablation mechanisms are comparable and both surpass the growth rate under the thermoelastic mechanism. This pattern is primarily due to dynamic adjustments in the ultrasonic wave directivity for longitudinal waves and changes in waveform polarity for surface waves. Conversely, the shear wave energy exhibits a more intricate three-stage linear variation trend, influenced by variations in ultrasonic wave directivity and step-like feature under different mechanisms. Specifically, there is a linear increase in energy under the thermoelastic mechanism, a decrease during the slight ablation stage, and a more pronounced linear growth under the ablation mechanism.

(2) With the incident pulsed laser energy held constant, the energy variation trends of both longitudinal and surface waves conform to a power-law function as the irradiation spot diameter decreases. In contrast, the behavior of the shear wave is more intricate across different mechanisms. Its ultrasonic energy gradually accumulates before stabilizing under the thermoelastic mechanism, dissipates rapidly under the slight ablation mechanism, and subsequently increases under the ablation mechanism.

(3) It is found that ultrasonic waveforms are not solely determined by laser power density. Even with high laser power density, a larger spot size may generate ultrasonic waveforms dominated by thermoelastic effects. This phenomenon is ascribed to the intensification of the thermoelastic effect with the proportional increase in laser irradiation spot area for a given laser power density.

(4) An approach is proposed to characterize grain size by evaluating the downshift in central frequency based on the signal spectrum at the arrival time of ultrasonic pulse peaks obtained via time-frequency analysis. The SCFRs of longitudinal and shear pulse echoes show linear relationships with grain size in polycrystalline materials. Consequently, grain size in metal materials can be precisely estimated by measuring the SCFR between two consecutive echoes in the time-frequency domain. When compared to frequency domain analysis, the standard deviation of the SCFR in the time-frequency domain is reduced by approximately 2/3. This suggests that time-frequency domain analysis offer greater stability and reduced volatility. Further investigation reveals that in samples with larger grain sizes ($d > 32$ μm), the SCFR of longitudinal waves is more pronounced than that of shear waves, with a grain size evaluation error below 4.03%, indicating excellent accuracy. Conversely, in fine-grained materials ($d < 32$ μm), the SCFR of shear waves is more prominent, resulting in a slightly smaller prediction error than longitudinal waves, approximately 4.84%.

This study enhances understanding of the laser-ultrasonic generation regime and the correlation between ultrasonic wave properties and microstructural grain sizes. It provides support for laser-ultrasonic detection and characterization of metallurgical characteristics in metals and alloys.

Acknowledgments

The work was supported in part by the Natural Science Foundation of Shandong Province, China (Grant No. ZR2023ME073), the National Natural Science Foundation of China (Grant No. 51805304), the Education Department of Shandong Province, China (Grant No. 2022KJ130), and Qilu University of Technology (Shandong Academy of

Sciences), China (Grant Nos. 2023PY009, 2021JC02008 and 2022GH005).

References

[1] Xie L Y, Lian Y D, Du F J, Wang Y L and Lu Z W 2024 *Opt. Laser Technol.* **176** 110876
[2] Sun G and Zhou Z 2014 *Optik* **125** 3608
[3] Ji B P, Zhang Q D, Cao J S, Li H and Zhang B Y 2021 *Optik* **226** 165893
[4] Davies S J, Edwards C, Taylor G S and Palmer S B 1993 *J. Phys. D: Appl. Phys.* **26** 329
[5] Garcin T, Schmitt J H and Militzer M 2016 *J. Alloys Compd.* **670** 329
[6] Davis G, Nagarajah R, Palanisamy S, Rashid RAR, Rajagopal P and Balasubra-maniam K 2019 *Int. J. Adv. Manuf. Technol.* **102** 2571
[7] Song Y F, Zi X H, Fu Y D, Li X B, Chen C and Zhou K C 2018 *Measurement* **118** 105
[8] Rose L R F 1984 *J. Acoust. Soc. Am.* **75** 723
[9] Doyle P A 1986 *J. Phys. D: Appl. Phys.* **19** 1613
[10] McDonald F A 1990 *Appl. Phys. Lett.* **56** 230
[11] Sanderson T, Charles U and Jacek J 1997 *Review of Progress in Quantitative Nondestructive Evaluation* (Berlin: Springer) chap. 16 pp. 601–607
[12] Sanderson T, Charles U and Jacek J 1998 *Ultrasonics* **35** 553
[13] Dewhurst R J, Hutchins D A, Palmer S B and Scruby C B 1982 *J. Appl. Phys.* **53** 4064
[14] Hutchins D A, Nadeau F and Cielo P 1986 *Can. J. Phys.* **64** 1334
[15] Xu W L, Zhang J, Li X H, Yuan S X, Ma G B, Xue Z X, Jing X C and Cao J C 2022 *NDT & E Int.* **125** 102548
[16] Aussel J D, Brun A L and Baboux J C 1988 *Ultrasonics* **26** 245
[17] Krylov V V 2016 *Ultrasonics* **69** 279
[18] Nakahata K, Sugahara H, Barth M, Kohler B and Schubert F 2016 *Ultrasonics* **67** 18
[19] Van P A, Huthwaite P, Brett C R and Lowe J S 2016 *NDT & E Int* **81** 9
[20] Choi S and Jhang K Y 2018 *J. Mech. Sci. Technol.* **32** 4191
[21] Zhou S, Reynolds P, Krause R, Buma T, O'Donnel M O and Hossack J A 2004 *IEEE Trans. Ultrason. Ferroelectr. Freq. Control* **51** 1178
[22] Cerniglia D, Pantano A and Mineo C 2011 *Appl. Phys. A* **105** 959
[23] Xu B, Shen Z, Ni X and Lu J 2004 *J. Appl. Phys.* **95** 2116
[24] Pyzik P, Ziaja-Sujdak A, Spytek J, O'Donnel M, Pelivanov I and Ambrozinski L 2021 *Photoacoustics* **21** 100226
[25] Aussel J D and Monchalin J P 1989 *Ultrasonics* **27** 165
[26] Dewhurst R J, Hutchins D A, Palmer S B and Scruby C B 1982 *J. Appl. Phys.* **53** 4064
[27] Quintero R, Simonetti F, Howard P, Friedl J and Sellinger A 2017 *NDT & E Int.* **88** 8
[28] Scruby C B, Dewhurst R J, Hutchins D A and Palmer S B 1980 *J. Appl. Phys.* **51** 6210
[29] Wang K, Wu M Y, Yan Z B, Li D R, Xin R L and Liu Q 2018 *J. Alloys Compd.* **752** 14
[30] Gil F J and Planell J A 2000 *Mater. Sci. Eng. A* **283** 17
[31] Morales R E, Harke K J, Tringe J W, Stobbe D M and Murray T W 2022 *Sci. Rep.* **12** 9865
[32] Choi S and Kyung Y J 2018 *J. Mech. Sci. Technol.* **32** 4191
[33] Dewhurst R J, Hutchins D A, Palmer S B and Scruby C B 1982 *J. Appl. Phys.* **53** 4064
[34] Scryby C B 1990 *Laser ultrasonics techniques and applications* 1st edn (New York: Boca Raton CRC Press) p. 301
[35] Lin J and Qu L S 2000 *J. Sound Vib.* **234** 135
[36] Zhang Q Z, Yang W and Zhang S B 2018 *Sensors* **18** 198
[37] Mesaros M, Martinez O E, Bilmes G M and Tocho J O 1997 *J. Appl. Phys.* **81** 1014
[38] Bai X, Zhao Y, Ma J, Guo R and Zhang H 2019 *Mat. Charact.* **155** 109800
[39] Stanke F E and Kino G S 1984 *J. Acoust. Soc. Am.* **75** 665
[40] Arguelles A P and Turner J A 2017 *J. Acoust. Soc. Am.* **141** 4347
[41] Kube C M and Turner J A 2015 *J. Acoust. Soc. Am.* **137** EL476